Measurement of the 70Ge(n, γ) cross section up to 300 keV at the CERN n_TOF facility

(n_TOF Collaboration) Gawlik, A.; ...; Bosnar, Damir; ...; Žugec, Petar

Source / Izvornik: **Physical Review C, 2019, 100**

Journal article, Published version
Rad u časopisu, Objavljena verzija rada (izdavačev PDF)

https://doi.org/10.1103/PhysRevC.100.045804

Permanent link / Trajna poveznica: https://urn.nsk.hr/urn:nbn:hr:217:858285

Measurement of the ^{70}Ge(n, γ) cross section up to 300 keV at the CERN n_TOF facility

A. Gawlik,[1] C. Lederer-Woods,[2,*] J. Andrzejewski,[1] U. Battino,[2] P. Ferreira,[3] F. Gunsing,[4,5] S. Heinitz,[6] M. Krtička,[7] C. Massimi,[8,9] F. Mingrone,[8] J. Perkowski,[1] R. Reifarth,[10] A. Tattersall,[2] S. Valenta,[7] C. Weiss,[5,11] O. Aberle,[5] L. Audouin,[12] M. Bacak,[11] J. Balibrea,[13] M. Barbagallo,[14] S. Barros,[3] V. Bécares,[13] F. Bečvář,[7] C. Beinrucker,[10] E. Berthoumieux,[4] J. Billowes,[15] D. Bosnar,[16] M. Brugger,[5] M. Caamaño,[17] F. Calviño,[18] M. Calviani,[5] D. Cano-Ott,[13] R. Cardella,[5] A. Casanovas,[18] D. M. Castelluccio,[19,8] F. Cerutti,[5] Y. H. Chen,[12] E. Chiaveri,[5] N. Colonna,[14] G. Cortés,[18] M. A. Cortés-Giraldo,[20] L. Cosentino,[21] L. A. Damone,[14,22] M. Diakaki,[4] M. Dietz,[2] C. Domingo-Pardo,[23] R. Dressler,[6] E. Dupont,[4] I. Durán,[17] B. Fernández-Domínguez,[17] A. Ferrari,[5] P. Finocchiaro,[21] V. Furman,[24] K. Göbel,[10] A. R. García,[13] T. Glodariu,[25] I. F. Gonçalves,[3] E. González-Romero,[13] A. Goverdovski,[26] E. Griesmayer,[11] C. Guerrero,[20] H. Harada,[27] T. Heftrich,[10] J. Heyse,[28] D. G. Jenkins,[29] E. Jericha,[11] F. Käppeler,[30] Y. Kadi,[5] T. Katabuchi,[31] P. Kavrigin,[11] V. Ketlerov,[26] V. Khryachkov,[26] A. Kimura,[27] N. Kivel,[6] I. Knapova,[7] M. Kokkoris,[32] E. Leal-Cidoncha,[17] H. Leeb,[11] J. Lerendegui-Marco,[20] S. Lo Meo,[19,8] S. J. Lonsdale,[2] R. Losito,[5] D. Macina,[5] J. Marganiec,[1] T. Martínez,[13] P. Mastinu,[33] M. Mastromarco,[14] F. Matteucci,[34,35] E. A. Maugeri,[6] E. Mendoza,[13] A. Mengoni,[19] P. M. Milazzo,[34] M. Mirea,[25] S. Montesano,[5] A. Musumarra,[21,36] R. Nolte,[37] A. Oprea,[25] N. Patronis,[38] A. Pavlik,[39] J. I. Porras,[5,40] J. Praena,[20,40] J. M. Quesada,[20] K. Rajeev,[41] T. Rauscher,[42,43] A. Riego-Perez,[18] P. C. Rout,[41] C. Rubbia,[5] J. A. Ryan,[15] M. Sabaté-Gilarte,[5,20] A. Saxena,[41] P. Schillebeeckx,[28] S. Schmidt,[10] D. Schumann,[6] P. Sedyshev,[24] A. G. Smith,[15] A. Stamatopoulos,[32] G. Tagliente,[14] J. L. Tain,[23] A. Tarifeño-Saldivia,[23] L. Tassan-Got,[12] A. Tsinganis,[32] G. Vannini,[8,9] V. Variale,[14] P. Vaz,[3] A. Ventura,[8] V. Vlachoudis,[5] R. Vlastou,[32] A. Wallner,[44] S. Warren,[15] M. Weigand,[10] C. Wolf,[10] P. J. Woods,[2] T. Wright,[15] and P. Žugec[16,5]

(The n_TOF Collaboration)[†]

[1]*University of Lodz, Lodz, Poland*
[2]*School of Physics and Astronomy, University of Edinburgh, Edinburgh, United Kingdom*
[3]*Instituto Superior Técnico, Lisbon, Portugal*
[4]*CEA Irfu, Université Paris-Saclay, F-91191 Gif-sur-Yvette, France*
[5]*European Organization for Nuclear Research (CERN), Geneva, Switzerland*
[6]*Paul Scherrer Institut (PSI), Villingen, Switzerland*
[7]*Charles University, Prague, Czech Republic*
[8]*Istituto Nazionale di Fisica Nucleare, Sezione di Bologna, Bologna, Italy*
[9]*Dipartimento di Fisica e Astronomia, Università di Bologna, Bologna, Italy*
[10]*Goethe University Frankfurt, Frankfurt, Germany*
[11]*Technische Universität Wien, Wien, Austria*
[12]*Institut de Physique Nucléaire, CNRS-IN2P3, Université Paris-Sud, Université Paris-Saclay, F-91406 Orsay Cedex, France*
[13]*Centro de Investigaciones Energéticas Medioambientales y Tecnológicas (CIEMAT), Madrid, Spain*
[14]*Istituto Nazionale di Fisica Nucleare, Sezione di Bari, Bari, Italy*
[15]*University of Manchester, Manchester, United Kingdom*
[16]*Department of Physics, Faculty of Science, University of Zagreb, Zagreb, Croatia*
[17]*University of Santiago de Compostela, Santiago de Compostela, Spain*
[18]*Universitat Politècnica de Catalunya, Barcelona, Spain*
[19]*Agenzia Nazionale per le Nuove Tecnologie (ENEA), Bologna, Italy*
[20]*Universidad de Sevilla, Sevilla, Spain*
[21]*INFN Laboratori Nazionali del Sud, Catania, Italy*
[22]*Dipartimento di Fisica, Università degli Studi di Bari, Bari, Italy*
[23]*Instituto de Física Corpuscular, CSIC - Universidad de Valencia, Valencia, Spain*
[24]*Joint Institute for Nuclear Research (JINR), Dubna, Russia*
[25]*Horia Hulubei National Institute of Physics and Nuclear Engineering, Bucharest-Magurele, Romania*
[26]*Institute of Physics and Power Engineering (IPPE), Obninsk, Russia*
[27]*Japan Atomic Energy Agency (JAEA), Tokai-mura, Japan*
[28]*European Commission, Joint Research Centre, Geel, Retieseweg 111, B-2440 Geel, Belgium*
[29]*University of York, York, United Kingdom*

[*]Corresponding author: claudia.lederer-woods@ed.ac.uk
[†]www.cern.ch/ntof

[30]*Karlsruhe Institute of Technology, Campus North, IKP, 76021 Karlsruhe, Germany*
[31]*Tokyo Institute of Technology, Tokyo, Japan*
[32]*National Technical University of Athens, Athens, Greece*
[33]*Istituto Nazionale di Fisica Nucleare, Sezione di Legnaro, Legnaro, Italy*
[34]*Istituto Nazionale di Fisica Nucleare, Sezione di Trieste, Trieste, Italy*
[35]*Dipartimento di Astronomia, Università di Trieste, Trieste, Italy*
[36]*Dipartimento di Fisica e Astronomia, Università di Catania, Catania, Italy*
[37]*Physikalisch-Technische Bundesanstalt (PTB), Bundesallee 100, 38116 Braunschweig, Germany*
[38]*University of Ioannina, Ioannina, Greece*
[39]*University of Vienna, Faculty of Physics, Vienna, Austria*
[40]*University of Granada, Granada, Spain*
[41]*Bhabha Atomic Research Centre (BARC), Mumbai, India*
[42]*Centre for Astrophysics Research, University of Hertfordshire, Hertfordshire, United Kingdom*
[43]*Department of Physics, University of Basel, Basel, Switzerland*
[44]*Australian National University, Canberra, Australia*

(Received 1 April 2019; published 17 October 2019)

Neutron capture data on intermediate mass nuclei are of key importance to nucleosynthesis in the weak component of the slow neutron capture processes, which occurs in massive stars. The (n, γ) cross section on ^{70}Ge, which is mainly produced in the *s* process, was measured at the neutron time-of-flight facility n_TOF at CERN. Resonance capture kernels were determined up to 40 keV neutron energy and average cross sections up to 300 keV. Stellar cross sections were calculated from $kT = 5$ keV to $kT = 100$ keV and are in very good agreement with a previous measurement by Walter and Beer (1985) and recent evaluations. Average cross sections are in agreement with Walter and Beer (1985) over most of the neutron energy range covered, while they are systematically smaller for neutron energies above 150 keV. We have calculated isotopic abundances produced in *s*-process environments in a 25 solar mass star for two initial metallicities (below solar and close to solar). While the low metallicity model reproduces best the solar system germanium isotopic abundances, the close to solar model shows a good global match to solar system abundances in the range of mass numbers $A = 60$–80.

DOI: 10.1103/PhysRevC.100.045804

I. MOTIVATION

The elemental abundances above Fe are mainly produced by two distinct neutron capture processes in stars and stellar explosions, the slow neutron capture process (*s* process) [1] and the rapid neutron capture process (*r* process) [2], while only about 1% of heavy element abundances is produced by charged particle and photoinduced reactions (*p* process) [3]. The *s* process occurs at moderate neutron densities of typically 10^7–10^{12} cm^{-3} and is characterized by a sequence of neutron captures followed by β decays [1]. Since radioactive decays are usually faster than neutron capture times, the reaction path proceeds along the line of stable nuclei. In massive stars (>8 solar masses $M_\odot$), the *s* process occurs in two different burning stages, towards the end of He core burning at temperatures of about 0.3 GK (1 GK $= 10^9$ K), and later during carbon shell burning, when temperatures reach 1 GK [4–8]. This so-called *weak* component of the *s* process produces dominantly elements between Fe and Zr, owed to the relatively low neutron exposures reached. The main component of the *s* process contributes dominantly abundances between Zr and Bi, and occurs in low and intermediate mass stars (about $1-5\,M_\odot$) during their asymptotic giant branch (AGB) phase [1,9].

In our cosmos, germanium is produced by more than one nucleosynthesis process; however, the bulk of it (about 80%) is thought to be produced by the weak *s* process in massive stars [10]. Around 12% is estimated to originate from the *main s* process in AGB stars, while only a few percent is produced by explosive nucleosynthesis processes, such as the *r* process, operating at very high neutron densities, and the α-rich freeze-out forming the Fe group nuclei at the end of a massive star's life. To disentangle the different contributions to observed germanium abundances in our solar system and stellar atmospheres, it is crucial to accurately determine the *s*-process contribution to germanium abundances. Figure 1 shows the *s*-process reaction path in the germanium mass region. ^{70}Ge occupies a special position: It is shielded from rapid neutron capture nucleosynthesis by the stable isobar ^{70}Zn, suggesting that ^{70}Ge is dominantly produced in the *s* process (hence it is a so-called *s*-only isotope), and its abundance thus can be used as an anchor point when comparing to observed isotopic abundances.

Neutron capture cross sections are a key nuclear physics input to calculate abundances produced in *s*-process nucleosynthesis. Since neutrons are rapidly thermalized in the stellar environment, the effective stellar cross section is a convolution of the energy dependent neutron capture cross section with a Maxwellian velocity distribution; thus, stellar neutron capture cross sections are called Maxwellian averaged cross sections (MACS). For *s*-process environments, MACS values need to be known up to kT values of about 90 keV, corresponding to the highest temperatures reached in the *s* process.

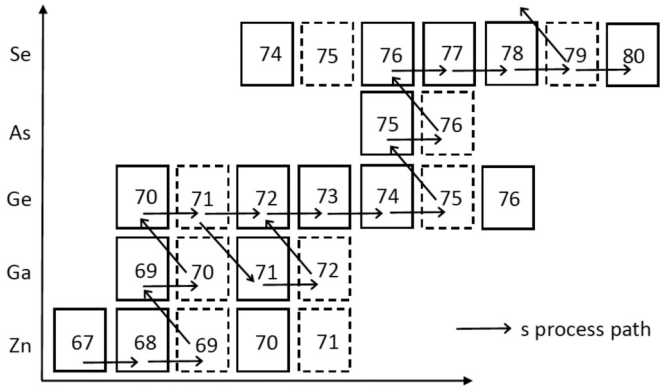

FIG. 1. Main nucleosynthesis path of the *s* process in massive stars during He core burning. Solid boxes represent stable, dashed boxes represent unstable isotopes.

Investigations using Monte Carlo variation of reaction rates to assess the impact of specific reactions on the final abundances predicted by stellar models have been performed recently. The reaction ^{70}Ge(n,γ) has been identified as a key reaction determining the uncertainty of ^{70}Ge in the main *s* process, both in the thermal pulse and in interpulse burning of AGB stars [11]. The reaction ^{70}Ge(n,γ) and the recently measured ^{73}Ge(n,γ) [12] were found to be key reactions for the abundances of ^{70}Ge and ^{73}Ge, respectively, in the enhanced weak *s* process occurring in rotating, metal-poor massive stars [13]. ^{73}Ge(n,γ) also appeared as key rate in the regular weak *s* process in the same study.

Existing experimental data on stellar neutron capture on germanium isotopes are scarce, which motivated a campaign at n_TOF to measure cross sections on all stable germanium isotopes [14]. Results on ^{73}Ge(n,γ) have recently been published and show that the germanium isotopic abundance pattern produced in the *s* process in a low metallicity massive star is consistent with the isotopic abundance pattern of our solar system [12]. This paper describes the study of the ^{70}Ge(n,γ) reaction. There are few experimental data available on this reaction in the keV neutron energy range; Walter and Beer [15] measured cross sections from 3 to 240 keV and calculated MACSs in the range $kT = 20$–50 keV. In addition, Maletski *et al.* [16] have published neutron resonance data on ^{70}Ge + *n* reactions for neutron energies up to 28.6 keV; however, partial radiative widths Γ_γ have only been determined for three low energy resonances, while for the remaining resonances only neutron widths Γ_n and resonance energies E_R are available. Harvey and Hockaday [17] have determined total cross sections for natural germanium, identifying several ^{70}Ge + *n* resonances up to 43 keV neutron energy. Evaluated ^{70}Ge(n,γ) cross sections recommended in major nuclear data libraries such as ENDF/B-VIII [18] and JENDL-4.0 [19] use experimental data by Maletski *et al.* and transmission data on natural germanium by Harvey and Hockaday for neutron energies below 14 keV, while for higher neutron energies evaluated cross sections are based on statistical parameters extracted from data at lower neutron energies.

This work provides neutron capture resonance data up to energies of 40 keV. In combination with average neutron capture cross sections determined for neutron energies up to 300 keV, we also calculated Maxwellian averaged cross sections for the entire range of astrophysical interest, from $kT = 5$ keV to $kT = 100$ keV.

II. MEASUREMENT

The measurement was performed at the neutron time-of-flight facility n_TOF at CERN [20]. At n_TOF, neutrons are produced by spallation reactions of a 20 GeV/c proton beam by the CERN Proton Synchrotron (PS) on a cylindrical 1.3 ton lead target (40 cm length, 60 cm diameter) [21]. The initially highly energetic neutrons are moderated using a combination of water and borated water layers surrounding the target (the former also cools the target). The resulting moderated neutron spectrum exhibits a nearly isolethargic energy dependence and ranges from thermal energies (25 meV) to several GeV. The proton beam is pulsed, with a time width of 7 ns r.m.s. and a repetition rate of about 0.8 Hz. At n_TOF, there are two experimental areas, at flight path lengths of 185 m (EAR-1) and 20 m (EAR-2). The ^{70}Ge(n,γ) measurement was performed at EAR-1, taking advantage of the excellent neutron energy resolution ranging from 3×10^{-4} at 1 eV to 3×10^{-3} at 100 keV [21].

The prompt emission of γ rays following neutron capture was detected with a set of four liquid scintillation detectors, filled with deuterated benzene (C_6D_6). These detectors are optimal for measurement of radiative neutron capture since they are almost insensitive to neutrons which are scattered from the capture sample. The detectors were arranged at angles of 125 degrees with respect to the neutron beam to minimise effects of anisotropic γ-ray emission for $\ell > 0$ states in the compound nucleus.

The ^{70}Ge(n,γ) reaction was studied using a highly enriched $^{70}GeO_2$ sample in cylindrical form. In addition, measurements were taken with a metallic germanium sample of natural composition to identify any contributions from other Ge isotopes present in the enriched sample, and with a Au sample which was used to normalize the neutron capture data (see Sec. III). The samples were glued on a thin mylar foil fixed to an Al ring. The background induced by the sample holder was measured by placing an empty sample holder in the beam. To keep any systematic effects due to sample positioning to a minimum, the samples were accurately centered on the holder using a jig and a hollow metallic cylinder aligned with the annular frame of the sample holder. Table I lists all samples and their characteristics used in the measurement.

Detector signals were recorded using 14-bit fast digitizers operated at a sampling rate of 1 GHz. Data acquisition was triggered by the pickup signal of the PS accelerator and for each neutron pulse data were recorded for a duration of 100 ms, corresponding to neutron energies of about 0.02 eV. Detector signal times and amplitudes were extracted for each neutron burst using an offline pulse shape algorithm [22].

TABLE I. Properties of the samples used in the experiment.

Sample	Chemical form	Mass (g)	Diameter (cm)	Sample composition (%)
^{70}Ge	GeO_2	2.705	2	^{70}Ge(97.71); ^{72}Ge(2.23); ^{73}Ge(0.02); ^{74}Ge(0.03); ^{76}Ge(0.01)
^{nat}Ge	metal	1.903	2	^{70}Ge(20.52); ^{72}Ge(27.45); ^{73}Ge(7.76); ^{74}Ge(36.52); ^{76}Ge(7.75)
^{197}Au	metal	0.664	2	^{197}Au (100)
Empty holder				

III. DATA ANALYSIS AND RESULTS

A. Time-of-flight to neutron energy conversion

The neutron time-of-flight spectra were converted to neutron energy using the relativistic relation

$$E_n = m_n c^2(\gamma - 1) \tag{1}$$

with

$$\gamma = \frac{1}{\sqrt{1-(L/t_f)^2/c^2}}, \tag{2}$$

where m_n is the mass of the neutron, L is the flight path length, and t_f is the neutron time of flight. The determination of t_f relies on accurate knowledge of the neutron production time. When the proton pulse hits the spallation target, a burst of γ rays and ultrarelativistic particles is produced alongside neutrons. This burst is called γ flash, and produces a short, high amplitude signal in the C_6D_6 detectors, allowing determination of the time of neutron production for each pulse with high accuracy. The flight path length L was determined using a Au sample in the beam. Au has several low energy resonances for which resonance energies have been accurately determined at the Joint Research Centre in Geel [23]. These are now included in the latest evaluated resonance data for ^{197}Au(n,γ) by ENDF/B-VIII [18]. The flight path has been fitted to reproduce the resonance energies for these well known resonances and was determined to be 183.94 ± 0.04 m.

B. Capture yield

The neutron capture yield as a function of neutron energy is obtained as

$$Y(E_n) = f_N(E_n)\frac{C(E_n) - B(E_n)}{\epsilon_c \Phi(E_n)}, \tag{3}$$

where C is the count spectrum of the enriched ^{70}Ge sample, B is the background, ϵ_c is the efficiency of detecting a capture event, and Φ is the neutron flux. The factor f_N is a normalization factor taking into account that the capture sample does not cover the entire size of the neutron beam. In the following subsections, the determination of each of those terms will be described.

1. Detection efficiency

The efficiency to detect the γ-ray emission after a neutron capture event depends on the deexcitation path of the compound nucleus, which in general varies from event to event. The total energy detection principle was used by combining the above-mentioned detection system with the pulse height weighting technique (PHWT) [24,25]. The total energy detection principle is applicable to detection systems of low efficiency, where at most one γ ray per capture event is detected. If the γ-ray detection efficiency is proportional to the γ-ray energy, i.e., $\epsilon_\gamma \propto E_\gamma$, it can be shown that the efficiency of detecting a capture event is proportional to the excitation energy of the compound system, i.e., $\epsilon_c \propto S_n + E_{cm}$, where S_n is the neutron separation energy and E_{cm} is the center-of-mass energy. To achieve $\epsilon_\gamma \propto E_\gamma$, the PHWT is used, where weighting factors are applied to each detected event, depending on their amplitude. These were determined in GEANT4 Monte Carlo simulations [26], simulating the detector response to mono-energetic γ-rays from 0.2 to 10.0 MeV. Simulations took into account the detailed geometry of the experimental setup and samples used, including the spatial distribution of the neutron beam, and neutron and γ-ray self absorption in the samples. The data further need to be corrected for a loss of γ rays below the detector threshold (200 keV) and for transitions without γ-ray emission (electron conversion). The correction for both Au and Ge was calculated using the code DICEBOX [27], that simulates individual capture cascades based on experimental information on low-lying levels and uses level density and photon strength function models at higher energies.

The systematic uncertainty of the neutron capture yield due to the PHWT is 2% [28].

2. Background subtraction

The background $B(E_n)$ consists of several components that need to be corrected for. Background unrelated to the neutron beam, due to ambient radioactivity and cosmic rays, is determined in beam-off runs and subtracted from the Au and Ge sample spectra. Background produced by neutron reactions with material in and around the beam line is measured by taking data with an empty sample holder.

Figure 2 shows the ^{70}Ge spectrum, compared to backgrounds due to the empty sample holder and due to ambient activity. Weighting functions have been applied to all these spectra, hence the figure shows weighted counts as a function of neutron energy. The empty sample holder contributes to background over the entire neutron energy range, while the ambient activity, which is constant in time, only contributes at low neutron energies. The third component is background related to the sample, specifically by neutrons scattered off the GeO_2 sample. These scattered neutrons may be captured in surrounding material and produce γ-ray cascades detected by the C_6D_6 system. The C_6D_6 detectors themselves are extremely insensitive to capturing neutrons [29,30], and therefore any background due to direct interaction of scattered

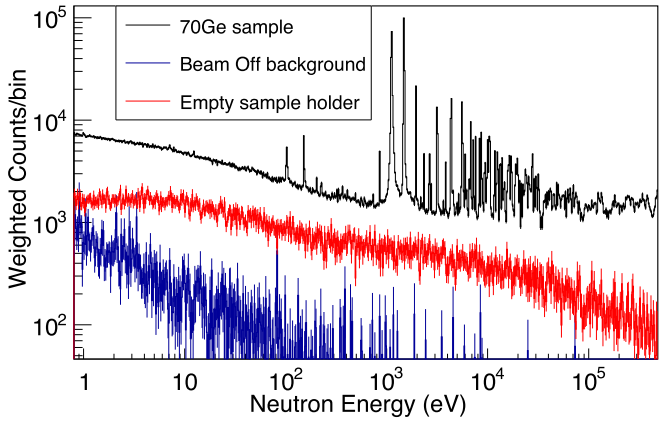

FIG. 2. Plot of the weighted Ge spectrum compared to empty sample holder and ambient background.

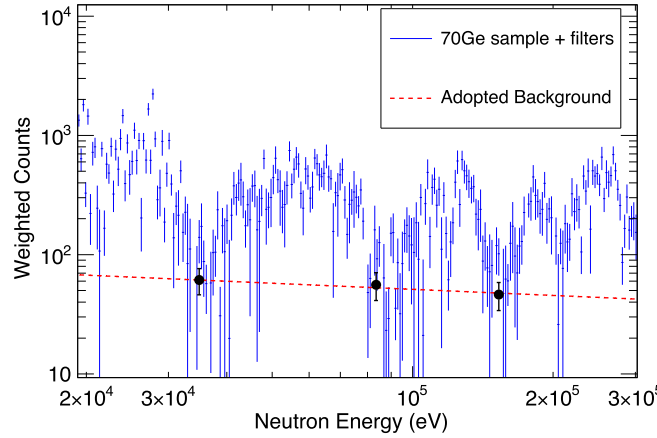

FIG. 3. Ge+filter spectrum (ambient and empty sample holder + filter spectrum subtracted), and background determined from filter dip minima.

neutrons with the detectors themselves can be neglected for the present measurement. While care has been taken to minimize material around the beam pipe and to use materials with low neutron cross sections, such as Al, there may be residual background due to neutrons scattered from the sample and being captured at a later time in structural material, such as the walls [31].

For the resonance region, individual neutron resonances were fitted including a flat, constant background to account for these backgrounds. For the unresolved resonance region, the background is determined using neutron filters. Neutron filters are materials in the beam line which absorb all neutrons at certain resonance energies. In the present case, an Al filter was used, with negligible transmission of neutrons at around 35, 86, and 150 keV neutron energy. Consequently, any counts in these filter dips must come from neutrons scattered off the sample and captured somewhere in the experimental area at a later time. This background was determined by measuring a Ge spectrum with filters and an empty sample holder spectrum with filters. After subtraction of the empty spectrum, the Ge+Al filter spectrum was scaled to the Ge spectrum to account for the overall loss of neutrons. A smooth function was fitted to the flat minima of the filter dips, and the resulting background was subtracted from the Ge spectrum. Figure 3 shows the ^{70}Ge + filter spectrum and the fitted background. The background was found to be at a level of 10–15% of the Ge spectrum. Due to uncertainties in the scaling factor applied to the Ge+filter spectrum, and low statistics in the filter dips, the resulting uncertainty of the capture yield in the unresolved resonance region is 4%.

3. Neutron flux and normalization

The neutron flux was measured using several different detection systems and reference reactions in a dedicated campaign. Measurements were performed with a set of silicon detectors, detecting tritons and α particles emitted in the ^{6}Li(n,t) reaction from a LiF sample. A micromegas detector was used to determine the neutron flux using the reference reactions ^{6}Li(n,t) and ^{235}U(n,f), and an ionisation chamber by Physikalisch Technische Bundesanstalt Braunschweig measured (n,f) reactions on ^{235}U. The data from all three detection systems were combined to determine an accurate neutron flux, which has a systematic uncertainty below 1% for neutron energies <3 keV, and of 3.5% between 3 keV and 1 MeV [32]. More details on the neutron flux evaluation at n_TOF can be found in Ref. [33].

A normalization factor f_N needs to be applied since the neutron beam is larger than the capture sample. In addition, such a factor corrects for any inaccuracies in determination of the solid angle covered by the C_6D_6 detectors. The saturated resonance technique [34] was applied to determine the normalization factor with high accuracy. In the present case, data were normalized to the well known 4.9-eV resonance in the ^{197}Au(n,γ) reaction. For this resonance, the capture cross section is much larger than neutron scattering ($\Gamma_\gamma/\Gamma_n \approx 8$ [18]). If the Au sample is chosen to be sufficiently thick, all neutrons at the resonance energy will be absorbed by the sample. In addition, due to the high ratio of capture/scattering almost all neutrons will be radiatively captured within the sample, even if their first interaction is elastic scattering. Thus, almost 100% of neutrons passing the capture sample produce a Au neutron capture cascade, providing an absolute normalisation point for the neutron capture yield at 4.9 eV neutron energy. The size of the neutron beam has a slight dependence on neutron energy. This dependence has been determined in Monte Carlo simulations of the neutron transport from the spallation target to the experimental area, and has been verified in beam profile measurements [21]. In the region of interest, the change in neutron beam size is at most 1.5%. This small correction was applied to the data. As the saturated resonance technique is insensitive to the precise individual resonance parameters for the 4.9-eV resonance, the systematic uncertainty, including possible small errors in sample positioning, is 1%.

C. Resonance analysis

Neutron resonances in the capture yield were fitted with the multilevel, multichannel *R*-matrix code SAMMY [35]. SAMMY

takes into account all experimental effects, such as multiple interaction events (multiple scattering) and self shielding, and the broadening of resonances due to thermal motion (Doppler broadening) and the resolution of the experimental setup. In addition, the full sample composition, including impurities, was taken into account.

Capture data themselves do not usually allow a reliable determination of individual resonance parameters, such as resonance spin J and partial neutron and radiative widths Γ_n and Γ_γ. In general, only energy and capture kernel k, defined as

$$k = g\frac{\Gamma_n\Gamma_\gamma}{\Gamma_n + \Gamma_\gamma}, \tag{4}$$

can be obtained reliably. The statistical factor g is given by

$$g = \frac{(2J+1)}{(2s+1)(2I+1)}, \tag{5}$$

where J is the resonance spin, the neutron spin $s = 1/2$, and the ground state spin of the target nucleus $I(^{70}\mathrm{Ge}) = 0^+$, hence in our case $g = (2J+1)/2$.

Resonance structures could be resolved up to neutron energies of 40 keV. However, from about 25 keV the analysis of individual resonance parameters became increasingly difficult, due to the worsening of the experimental resolution combined with lower statistics and increasing natural resonance widths. For this reason, an averaged cross section was determined from 25 keV onwards (see Sec. III D).

Resonance energies and capture kernels k are shown in Tables II and III for neutron resonance energies below and above 25 keV, respectively. Examples of resonance fits in various neutron energy ranges are shown in Fig. 4. Uncertainties in Tables II and III are fit uncertainties only.

Systematic uncertainties in the capture kernels are due to the PHWT (2%), the normalization (1%), the neutron flux (1% for $E_n < 3$ keV, 3.5% for $E_n > 3$ keV), and the sample enrichment (1%). This amounts to total systematic uncertainties of 2.7% below and 4.3% above 3 keV neutron energy, respectively. In total, we fitted 110 resonances up to energies of 40 keV, of which 90 were not listed in previous evaluations.

Average resonance parameters, namely the average radiative width $\overline{\Gamma}_\gamma$ and the average resonance spacing D_0, were determined using the resonances below 25 keV assuming there are no unresolved doublets. There are 35 strong resonances for which the SAMMY fit yielded $\Gamma_n > 10 \times \Gamma_\gamma$. As $k \approx g\Gamma_\gamma$ for these resonances, we used the kernels determined from n_TOF data and the spins from a transmission measurement [17] to estimate the distribution of individual Γ_γ values in terms of the average radiative width $\overline{\Gamma}_\gamma$ and the width of the distribution σ_{Γ_γ}. Using the same method as in Ref. [12], namely the maximum likelihood fit assuming a Gaussian distribution of Γ_γ values, we obtained $\overline{\Gamma}_\gamma = 205(12)$ meV and $\sigma_{\Gamma_\gamma} = 70(10)$. Our value of the average radiative width is compatible with the literature values 185(30) meV [36] and 185(50) meV [37].

To determine D_0 we have adopted the neutron strength functions for s-, p-, and d-wave neutrons $S_0 = 2.1\times10^{-4}$, $S_1 = 1.5\times10^{-4}$, and $S_2 = 3\times10^{-4}$, and channel radius of 7 fm from Ref. [36]. The numbers of observed resonances above certain thresholds in the resonance kernel were compared to the simulated resonance sequences assuming the validity of the statistical model as in Ref. [38]. Our data are perfectly consistent with $D_0 = 830(100)$ eV; this value is compatible within 2σ with the literature value of 1170(230) eV [36,37].

Present values of D_0 and $\overline{\Gamma}_\gamma$ in combination with adopted S_0 and S_1 imply that the neutron width of the strongest p-wave resonances can reach the values of the strongest s-wave resonances already at E_n of a few keV. The determination of S_0 and S_1 without firm ℓ assignment is thus impossible; we can merely state that the literature values are reasonable. For example, simulations with a half value of S_1 during the

TABLE II. Resonance energies E_R and kernels k up to 25 keV determined with SAMMY. The uncertainties listed are from the fitting procedure.

E_R (eV)	k (meV)	E_R (eV)	k (meV)
152.38 ± 0.01	0.058 ± 0.002	12655.7 ± 0.3	148.4 ± 5.1
1118.4 ± 0.1	150.5 ± 5.7	13270.0 ± 4.6	206 ± 13
1474.23 ± 0.01	140.9 ± 0.9	13326.1 ± 0.4	168.2 ± 8.3
1484.17 ± 0.02	11.5 ± 0.2	13867.8 ± 0.6	194 ± 11
1514.23 ± 0.02	24.0 ± 0.2	13887.7 ± 1.0	47.2 ± 5.1
1953.16 ± 0.02	29.8 ± 0.4	14331.7 ± 0.5	121.7 ± 5.7
2358.51 ± 0.06	7.6 ± 0.2	14800.6 ± 0.5	117.2 ± 5.9
2652.83 ± 0.07	9.8 ± 0.3	15118.2 ± 1.0	30.6 ± 2.6
3170.27 ± 0.04	46.6 ± 0.8	15705.2 ± 0.8	223.8 ± 8.9
3224.02 ± 0.05	24.2 ± 0.5	16005.8 ± 0.4	326 ± 10
3846.2 ± 0.1	11.5 ± 0.4	16366.6 ± 0.6	222 ± 15
3853.7 ± 0.3	3.5 ± 0.3	16402.7 ± 0.8	136.5 ± 7.9
4290.40 ± 0.05	60.3 ± 1.0	16900.8 ± 0.6	183.9 ± 8.8
4397.5 ± 0.1	150.5 ± 2.1	17032.8 ± 0.7	268 ± 17
5157.0 ± 0.3	5.8 ± 0.4	17358.1 ± 0.4	225 ± 12
5530.9 ± 0.1	45.5 ± 1.2	17706.4 ± 1.0	45.5 ± 3.6
5602.0 ± 0.5	271.0 ± 4.2	17937.0 ± 1.1	41.1 ± 3.9
6035.6 ± 0.1	45.6 ± 2.5	18614.7 ± 3.1	186.3 ± 9.7
6590.8 ± 0.3	17.2 ± 0.9	18963.9 ± 0.6	362 ± 28
6796.8 ± 0.3	232.4 ± 4.0	19319.4 ± 0.5	278 ± 12
7259.7 ± 0.1	120.5 ± 4.8	19654.5 ± 0.8	254 ± 28
7591.0 ± 0.2	99.8 ± 4.0	19809.1 ± 0.6	209 ± 11
7669.2 ± 0.2	36.8 ± 1.5	20123.7 ± 1.4	59.3 ± 5.2
8289.2 ± 0.1	154.4 ± 5.2	20272.3 ± 0.7	278 ± 14
8663.9 ± 0.6	41.2 ± 3.3	20714.5 ± 0.9	159.7 ± 7.8
8699.4 ± 1.2	208.8 ± 6.8	20883.5 ± 1.1	88.6 ± 6.4
8723.5 ± 0.4	67.5 ± 4.2	21669.4 ± 5.1	117 ± 22
9395.9 ± 0.2	148.5 ± 6.7	21697.9 ± 0.9	127 ± 58
9957.0 ± 1.4	241.5 ± 6.9	22276.3 ± 0.8	267 ± 26
10018.5 ± 0.4	56.0 ± 3.3	22734.8 ± 2.4	188 ± 12
10118.2 ± 0.4	42.7 ± 2.2	23128.7 ± 1.0	190 ± 12
10367.6 ± 1.2	242.8 ± 7.6	23556.7 ± 1.6	53.9 ± 6.3
10505.0 ± 0.2	237.4 ± 7.7	23775.1 ± 1.5	150.1 ± 9.8
11648.7 ± 0.6	28.4 ± 2.1	23916.7 ± 0.8	440 ± 32
11838.5 ± 0.3	232.0 ± 6.9	24065.4 ± 3.9	167 ± 13
12310.0 ± 0.5	46.4 ± 2.9	24685.1 ± 0.9	329 ± 15
12399.2 ± 0.2	253.0 ± 8.6		

TABLE III. Resonance energies E_R and kernels k from 25 keV determined with SAMMY. The uncertainties listed are from the fitting procedure. Some of these resonances may be more complex structures, which could not be separated due to the worsening of the experimental resolution and the increasing natural resonance widths.

E_R (eV)	k (meV)	E_R (eV)	k (meV)
25011.8 ± 2.1	101.5 ± 8.3	32543.6 ± 2.4	125 ± 12
25348.5 ± 1.0	293 ± 16	32768.1 ± 3.8	94 ± 12
25656.7 ± 1.5	94.2 ± 8.9	34382.1 ± 3.1	212 ± 23
25857.2 ± 2.2	111 ± 10	34681.5 ± 7.3	121 ± 21
26039.4 ± 6.6	272 ± 19	35260 ± 16	121 ± 30
26670.5 ± 1.1	358 ± 16	35605.1 ± 7.1	456 ± 49
26925.8 ± 2.2	115 ± 10	35939.2 ± 5.9	88 ± 21
27264.4 ± 1.0	554 ± 56	36198.9 ± 3.1	423 ± 49
27706.5 ± 1.1	320 ± 17	36266.2 ± 2.7	330 ± 40
27892.9 ± 2.1	402 ± 21	36585 ± 15	219 ± 35
28137.4 ± 2.0	254 ± 15	37033.5 ± 7.0	207 ± 30
29161.1 ± 2.4	493 ± 32	37185.2 ± 3.8	343 ± 33
30035.2 ± 1.4	381 ± 19	37517.4 ± 3.0	347 ± 50
30294.4 ± 2.3	181 ± 12	37864.3 ± 3.1	208 ± 24
30666.4 ± 1.3	360 ± 16	38332.3 ± 8.5	146 ± 25
31629.6 ± 2.4	116 ± 13	38507.7 ± 3.7	177 ± 18
31845.7 ± 1.4	388 ± 27	39004.6 ± 6.2	464 ± 200
32047.7 ± 2.4	208 ± 18	39871.6 ± 5.6	315 ± 39
32405.2 ± 6.6	172 ± 22		

procedure of obtaining D_0 yielded inconsistent D_0 values for different adopted thresholds.

D. Unresolved resonance region

The threshold for observing individual resonances increases with energy, and from about 25 keV a non-negligible fraction of smaller resonances is missed, which would result in an underestimation of the cross section. Therefore, we determined an averaged neutron capture cross section between 25 and 300 keV from the neutron capture yield. The capture yield was corrected for multiple scattering and self-shielding effects using a Monte Carlo code which takes into account the sample composition and geometry as well as neutron scattering and capture cross sections. These corrections to the yield amounted to 6-7%. A conservative estimate of 20% uncertainty in these corrections results in a 1.4% uncertainty of the corrected neutron capture yield.

The unresolved cross section was obtained after subtraction of backgrounds due to neutron scattering (see Sec. III B 2) and contributions due to impurities. In the present case, the main impurity in the sample is ^{72}Ge with a content of 2.23%. Other germanium isotopes as well as oxygen in the sample have negligible contributions to the measured capture yield, either because of their low abundance in the sample or because of their small cross sections. We used ENDF/B-VIII [18] cross sections to estimate the contribution of the ^{72}Ge impurity to the measured cross section, yielding a background at a level of 1–2%. At present there is no experimental information on the ^{72}Ge(n,γ) cross section in the relevant energy range, and the cross section recommended by the ENDF/B-VIII

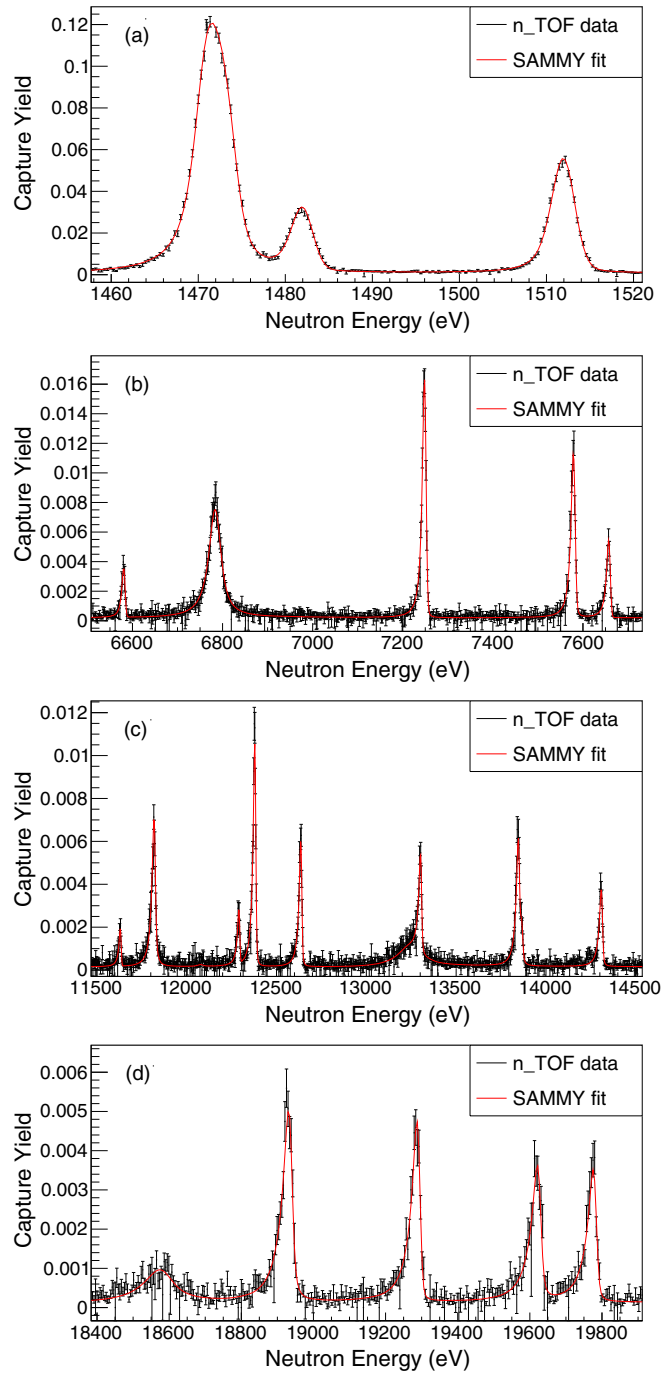

FIG. 4. (a)–(d) Examples for some SAMMY fits of the experimental capture yield.

evaluation is based on average resonance parameters obtained at lower neutron energies by Maletski *et al.* [16]. Assuming a 20% uncertainty in the ^{72}Ge cross section, the contribution to the uncertainty in the ^{70}Ge(n,γ) cross section is at most 0.4%. Total systematic uncertainties of the unresolved cross section are 6%, consisting of 4.3% systematic uncertainty as outlined in Sec. III C, the background subtraction with neutron filters (4%), correction for sample impurities (0.4%), and multiple scattering and self-shielding corrections (1.4%). Figure 5 shows a plot of the unresolved cross section obtained

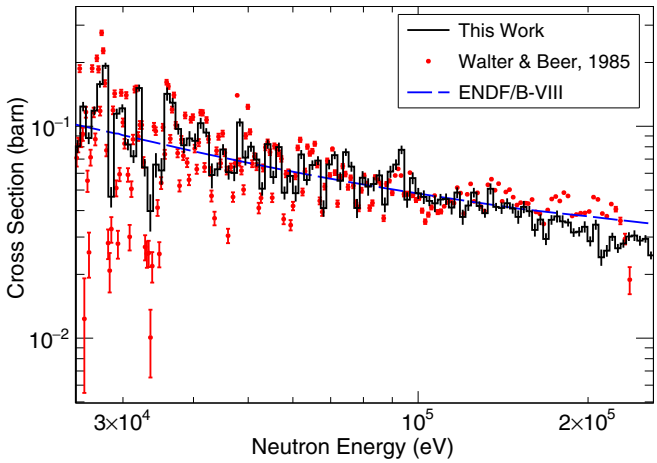

FIG. 5. Neutron capture cross section with statistical uncertainties in the unresolved resonance region from 25 to 300 keV. The data obtained in this work are compared to experimental results by Walter and Beer [15] and the ENDF/B-VIII evaluation [18].

in this work, compared to experimental results by Walter and Beer [15], and evaluated cross sections published in the ENDF/B-VIII library. The cross sections determined in this work are in fair agreement with Walter and Beer as well as ENDF/B-VIII over most of the neutron energy range covered, while they are systematically smaller than ENDF/B-VIII and Walter and Beer above 150 keV.

IV. STELLAR CROSS SECTIONS AND ASTROPHYSICAL IMPLICATIONS

Maxwellian averaged cross sections were determined by combining the cross section obtained from resonance parameters up to 25 keV neutron energy (resolved resonance region, RRR), with the unresolved averaged cross section for neutron energies between 25 and 300 keV (unresolved resonance region, URR). From 300 keV, we used cross sections recommended by the ENDF/B-VIII evaluation, but scaled by a factor 0.8 to take into account that the new experimental data indicate an overestimation of the cross section at higher neutron energies of 10–35%. MACS values were calculated for kT values between 5 and 100 keV using the formula

$$\mathrm{MACS} = \frac{2}{\sqrt{\pi}}\frac{1}{(kT)^2}\int_0^\infty E\sigma(E)\exp\left(-\frac{E}{kT}\right)dE. \quad (6)$$

Uncertainties taking into account all three components were determined in the following way: The common (absolute) uncertainty for RRR + URR MACSs $\sigma_{\mathrm{RRR+URR}}$ is due to the weighting procedure (2%), the sample enrichment (1%), the neutron flux (3.5%), normalization (1%), and counting statistics including uncertainties of the resonance fits (1%). An additional uncertainty just applicable to the URR, σ_{URR}, comes from the background subtraction using filters (4%), self-shielding and multiple scattering (1.4%), and subtraction of the ^{72}Ge background (0.4%). We have assigned a 20% uncertainty to the scaled ENDF/B-VIII cross sections (σ_{ENDF}) that were used for $E_n > 300$ keV. The contribution of cross sections above 300 keV to the MACS is negligible for kT values below 50 keV, and between 2% and 11% for kT = 60–100 keV. The total uncertainty of the MACS was then determined as

$$\sigma_{\mathrm{tot}} = \sqrt{\sigma^2_{\mathrm{RRR+URR}} + \sigma^2_{\mathrm{URR}} + \sigma^2_{\mathrm{ENDF}}}. \quad (7)$$

Hence, total uncertainties for MACSs values vary from 4.4% at $kT = 5$ keV to 5.6% at $kT = 100$ keV.

TABLE IV. Maxwellian averaged cross sections obtained from resonance data below, and averaged cross sections above, 25 keV neutron energy. The uncertainty is the total uncertainty, including systematic and statistical uncertainties.

	MACS (mb)		
kT (keV)	This work	KADoNiS-1.0 [39]	Walter and Beer [15]
5	212.4 ± 9.3	207.3	
10	159.7 ± 7.1	154.8	
20	115.8 ± 5.6	109.8	112 ± 6
30	94.2 ± 4.9	89.1 ± 5.0	92 ± 5
40	80.8 ± 4.3	77.1	81 ± 5
50	71.5 ± 3.9	69.3	75 ± 4
60	64.6 ± 3.6	63.7	
70	59.3 ± 3.3		
80	55.1 ± 3.0	56.2	
90	51.7 ± 2.9		
100	48.9 ± 2.7	51.4	

Table IV lists MACS values determined in this work from $kT = 5$ to 100 keV. MACSs in this work are compared to recommended values in the Karlsruhe Astrophysical Database of Nucleosynthesis in Stars (KADoNiS) version 1.0 [39], which is widely used as a reference for reaction rates in astrophysical calculations, and experimental MACSs determined by Walter and Beer [15]. Agreement with Walter and Beer values is very good, and there is also good agreement with KADoNiS-1.0, considering uncertainties. The trend of the MACS values with kT is flatter for Walter and Beer, which can be explained by their higher averaged cross section at high neutron energies.

Because ^{70}Ge is an even-even nucleus, the contribution of reactions on excited target states in the stellar plasma is negligible up to plasma temperatures of about 1.5 GK, which is well above the *s*-process temperature range [40,41]. Therefore the experimentally determined MACS can directly be used as stellar MACS in astrophysical calculations for the *s* process.

We have calculated *s*-process nucleosynthesis abundances for a massive $25M_\odot$ star for two initial metallicities, below solar ($z = 0.006$) and close to solar metallicity ($z = 0.01$),[1] using the multizone post-processing code MPPNP [42]. The neutron capture network, which is largely based on rates recommended in the latest released version of KADoNiS, KADoNiS-v0.3 [39], included the new ^{70}Ge(n,γ) MACSs obtained in this work and recent results from ^{73}Ge(n,γ) [12]. Due to the very good agreement with previous results, there

[1] z is defined as the mass fraction of elements heavier than helium; solar metallicity is $z_\odot = 0.014$.

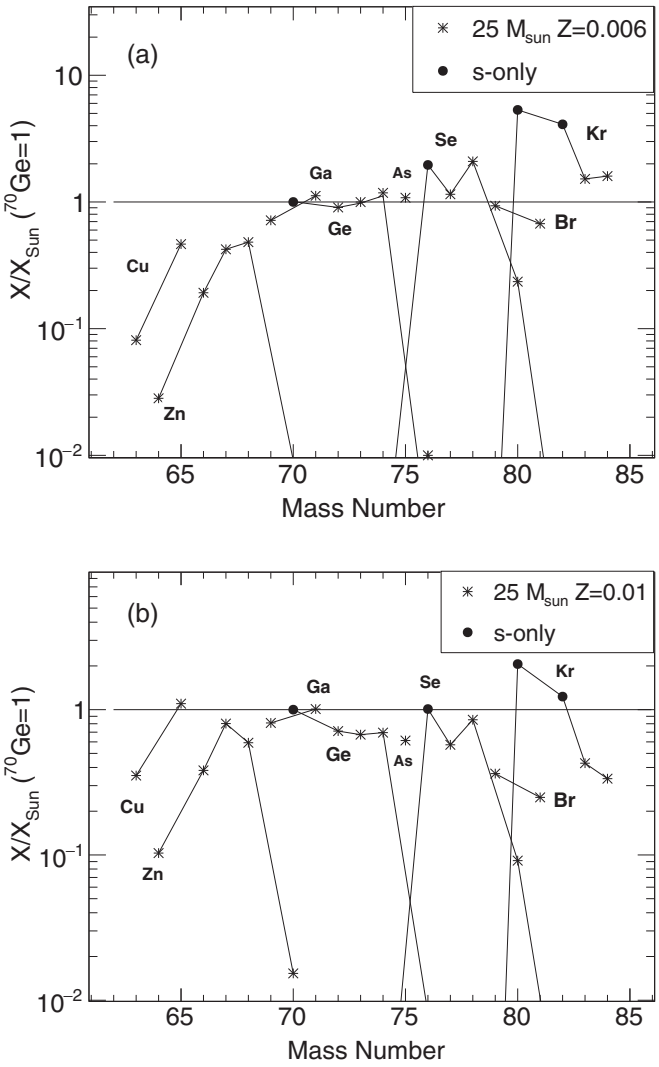

FIG. 6. Abundances produced in a $25M_{\odot}$ star for two initial metallicities z, normalized to solar system abundances for which contributions from the main s process and p process have already been subtracted. The distribution has been normalized to ^{70}Ge. s-only isotopes are shown as full circles and isotopes of the same element are connected by solid lines. The $z = 0.006$ metallicity model produces germanium isotopic abundances close to solar proportions, while the $z = 0.01$ model provides a better global fit for $A = 60$–80.

are only small changes in the resultant ^{70}Ge abundances produced in massive stars (about 3%) using the new ^{70}Ge MACS. However, our data provide an independent confirmation of the only previous measurement at stellar energies and, in addition, include also MACS for $kT > 50$ keV, thus improving the accuracy of stellar model predictions.

Figure 6 shows the *weak* s-process abundances produced before supernova explosion, scaled to solar system abundances and normalized to ^{70}Ge. Isotopes of the same element have been connected by solid lines. Contributions to the solar system abundances due to the *main* s process and the p process have been subtracted using results by Arlandini *et al.* [43] and Travaglio *et al.* [44], respectively. The absolute contributions of these two nucleosynthesis processes have been determined by normalizing to the *main* s-only isotope ^{150}Sm and p-only isotope ^{84}Sr, respectively. Hence, the solar system abundances shown in Fig. 6 only contain contributions from the *weak* s process and explosive nucleosynthesis processes (r process and α-rich freeze-out). The results show that the $z = 0.006$ model reproduces best the solar isotopic abundance pattern of germanium isotopes, while the model close to solar metallicity ($z = 0.01$) provides a better global fit to the other s-only isotopes ^{76}Se, ^{80}Kr, and ^{82}Kr. Furthermore, the $z = 0.01$ model indicates that the *weak* s process contributes a large fraction to solar ^{65}Cu, ^{67,68}Zn, ^{69,71}Ga, ^{72,73,74}Ge, ^{75}As, and ^{77,78}Se abundances. For a firm conclusion about the absolute contribution of the *weak* s process, however, stellar nucleosynthesis calculations using the new cross sections need to be implemented into calculations of galactic chemical evolution, taking into account stars of different initial metallicities and masses as well as contributions from explosive nucleosynthesis processes during core collapse supernova explosions.

V. SUMMARY

We measured ^{70}Ge(n,γ) cross sections up to 300 keV neutron energy at the neutron time-of-flight facility n_TOF at CERN. Resonance capture kernels of 110 resonances were determined up to 40 keV, while averaged cross sections were determined up to 300 keV. Maxwellian averaged cross sections were calculated and are in very good agreement with the only other previous measurement of this reaction at stellar energies [15], providing an important independent confirmation of stellar cross sections used in astrophysical calculations. The new MACSs combined with recent results for MACSs on ^{73}Ge(n,γ) [12] were used to calculate abundances produced in two massive star models, with subsolar and close-to-solar metallicity. Abundances for s-only isotopes match reasonably well with solar system values, in particular for the model close to solar metallicity, while the $z = 0.006$ model reproduces the germanium isotopic abundance pattern in our solar system.

ACKNOWLEDGMENTS

This work was supported by the Austrian Science Fund FWF (Grant No. J3503), the Adolf Messer Foundation (Germany), the UK Science and Facilities Council (Grant No. ST/M006085/1), and the European Research Council ERC-2015-StG Grant No. 677497. We also acknowledge support of Narodowe Centrum Nauki (NCN) (Grant No. UMO-2016/22/M/ST2/00183) and from MSMT of the Czech Republic and the Croatian Science Foundation under the Project No. IP-2018-01-8570.

[1] R. Reifarth, C. Lederer, and F. Käppeler, J. Phys. G **41**, 053101 (2014).

[2] F. Thielemann *et al.*, Prog. Part. Nuc. Phys. **66**, 346 (2011).

[3] T. Rauscher *et al.*, Rep. Prog. Phys. **76**, 066201 (2013).
[4] J. G. Peters, Astrophys. J. **154**, 225 (1968).
[5] R. G. Couch, A. B. Schmiedekamp, and W. D. Arnett, Astroph. J. **190**, 95 (1974).
[6] S. A. Lamb, W. M. Howard, J. W. Truran, and I. Iben, Astrophys. J. **217**, 213 (1977).
[7] C. M. Raiteri, M. Busso, G. Picchio, and R. Gallino, Astrophys. J. **371**, 665 (1991).
[8] C. M. Raiteri, M. Busso, G. Picchio, R. Gallino, and L. Pulone, Astrophys. J. **367**, 228 (1991).
[9] F. Herwig, Annu. Rev. Astron. Astrophys. **43**, 435 (2005).
[10] M. Pignatari, R. Gallino, M. Heil, M. Wiescher, F. Käppeler, F. Herwig, and S. Bisterzo, Astrophys. J. **710**, 1557 (2010).
[11] G. Cescutti, R. Hirschi, N. Nishimura, J. W. den Hartogh, T. Rauscher, A. St.J. Murphy, and S. Cristallo, Mon. Not. R. Astron. Soc. **478**, 4101 (2018).
[12] C. Lederer-Woods *et al.* (the n_TOF Collaboration), Phys. Lett. B **790**, 458 (2019).
[13] N. Nishimura, R. Hirschi, T. Rauscher, A. St. J. Murphy, and G. Cescutti, Mon. Not. R. Astron. Soc. **469**, 1752 (2017).
[14] C. Lederer *et al.*, Proposal to the ISOLDE and neutron time-of-flight committee, CERN Report No. CERN-INTC-2014-035; INTC-CLL-014 (CERN, Geneva, 2014), https://cds.cern.ch/record/1645832?ln=en.
[15] G. Walter and H. Beer, Astron. Astrophys. **142**, 268 (1985).
[16] K. Maletski, L. B. Pikelner, I. M. Salamatin, and E. I. Sharapov, Sov. At. Energ. **24**, 207 (1968).
[17] J. A. Harvey and M. Hockaday, EXFOR Entry 13770.004, https://www-nds.iaea.org/exfor/servlet/X4sGetSubent?reqx=11713&subID=13770004&plus=2.
[18] D. A. Brown *et al.*, Nucl. Data Sheets **148**, 1 (2018).
[19] K. Shibata *et al.*, J. Nucl. Sci. Technol. **48**, 1 (2011).
[20] www.cern.ch/ntof.
[21] C. Guerrero *et al.* (the n_TOF Collaboration), Eur. Phys. J. A **49**, 27 (2013).
[22] P. Zugec *et al.* (the n_TOF Collaboration), Nucl. Instrum. Methods A **812**, 134 (2016).
[23] C. Massimi *et al.*, J. Kor. Phys. Soc. **59**, 1689 (2011).
[24] R. L. Macklin and R. H. Gibbons, Phys. Rev. **159**, 1007 (1967).
[25] P. Schillebeeckxs *et al.*, Nucl. Data Sheets **113**, 3054 (2012).
[26] S. Agostinelli *et al.* (Geant4 Collaboration), Nucl. Instrum. Methods Phys. Res. A **506**, 250 (2003).
[27] F. Bečvář, Nucl. Instrum. Methods A **417**, 434 (1998).
[28] U. Abbondanno *et al.* (the n_TOF Collaboration), Nucl. Instrum. Methods Phys. Res. A **521**, 454 (2004).
[29] R. Plag, M. Heil, F. Käppeler, P. Pavlopulos, R. Reifarth, and K. Wisshak, Nucl. Instrum. Methods Phys. Res. A **496**, 425 (2003).
[30] P. Mastinu *et al.*, New C_6D_6 detectors: reduced neutron sensitivity and improved safety, CERN Reports No. n_TOF-PUB-2013-002 and No. CERN-n_TOF-PUB-2013-002, 2013, https://cds.cern.ch/record/1558147?ln=en.
[31] P. Zugec *et al.* (the n_TOF Collaboration), Nucl. Instrum. Methods A **760**, 57 (2014).
[32] M. Sabaté-Gilarte, M. Barbagallo *et al.* (the n_TOF Collaboration), n_TOF Collaboration Meeting, Catania, May 2016 (unpublished).
[33] M. Barbagallo *et al.* (the n_TOF Collaboration), Eur. Phys. J. A **49**, 156 (2013).
[34] R. L. Macklin, J. Halperin, and R. R. Winters, Nucl. Instrum. Methods **164**, 213 (1979).
[35] N. M. Larson, Updated users guide for SAMMY: Multilevel R-matrix fits to neutron data using Bayes' equations, Oak-Ridge National Laboratory, Technical Report No. ORNL/TM-9179/R8, 2008 (unpublished).
[36] S. F. Mughabghab, *Atlas of Neutron Resonances* (Elsevier, Amsterdam, 2006).
[37] R. Capote *et al.*, Nucl. Data Sheets **110**, 3107 (2009).
[38] J. Lerendegui-Marco *et al.*, Phys. Rev. C **97**, 024605 (2018).
[39] The Karlsruhe Astrophysical Database of Nucleosynthesis in Stars 1.0 (test version), online at https://exp-astro.de/kadonis1.0/, latest release KADoNiS-0.3; I. Dillmann, M. Heil, F. Käppeler, R. Plag, T. Rauscher, F. K. Thielemann, in *Capture Gamma-Ray Spectroscopy and Related Topics: 12th International Symposium*, September 2005, Notre Dame, IN, edited by A. Woehr and A. Aprahamian, AIP Conf. Proc. No. 819 (AIP, New York, 2006), p. 123.
[40] T. Rauscher, Astrophys. J. Suppl. **201**, 26 (2012).
[41] T. Rauscher, Astrophys. J. Lett. **755**, L10 (2012); **864**, L40 (2018).
[42] F. Herwig *et al.*, PoS (NIC X) **053**, 023 (2009).
[43] C. Arlandini *et al.*, Astrophys. J. **525**, 886 (1999).
[44] C. Travaglio *et al.*, Astrophys. J. **739**, 93 (2011).